ARTICLE IN PRESS

Nuclear Engineering and Technology xxx (xxxx) xxx

Contents lists available at ScienceDirect

Nuclear Engineering and Technology

journal homepage: www.elsevier.com/locate/net

Original Article

TEM investigation of helium bubble evolution in tungsten and ZrC-strengthened tungsten at 800 and 1000°C under 40keV He^+ irradiation

I. Ipatova [a,*], G. Greaves [b], D. Terentyev [c], M.R. Gilbert [a], Y.-L. Chiu [d]

[a] Culham Centre for Fusion Energy, United Kingdom Atomic Energy Authority, Culham Science Centre, Abingdon, OX14 3DB, United Kingdom
[b] School of Computing and Engineering, University of Huddersfield, Huddersfield, HD1 3DH, United Kingdom
[c] Belgium Nuclear Research Center, NMS unit, Boeretang 200, Mol B2400, Belgium
[d] School of Metallurgy and Materials, University of Birmingham, Elms Road, Birmingham, B15 2SE, United Kingdom

ARTICLE INFO

Keywords:
Tungsten
Zirconium carbide
Plasma-facing materials
In-situ helium exposure
Faceted helium bubbles
Transmission electron microscopy

ABSTRACT

Helium-induced defect nucleation and accumulation in polycrystalline W and W0.5 wt%ZrC (W0.5ZrC) were studied in-situ using the transmission electron microscopy (TEM) combined with 40 keV He^+ irradiation at 800 and 1000°C at the maximum damage level of 1 dpa. Radiation-induced dislocation loops were not observed in the current study. W0.5ZrC was found to be less susceptible to irradiation damage in terms of helium bubble formation and growth, especially at lower temperature (800 °C) when vacancies were less mobile. The ZrC particles present in the W matrix pin the forming helium bubbles via interaction between C atom and neighbouring W atom at vacancies. This reduces the capability of helium to trap a vacancy which is required to form the bubble core and, as a consequence, delays, the bubble nucleation.

At 1000 °C, significant bubble growth occurred in both materials and all the present bubbles transitioned from spherical to faceted shape, whereas at 800 °C, the faceted helium bubble population was dominated in W.

1. Introduction

While fusion energy is entering the age of delivery, developing materials that are capable to withstand the high heat loads and high neutron fluxes, and tritium permeation predicted for the divertor, and reactor-vessel walls is one of the main scientific challenges. Tungsten has traditionally stood out as an armour material for plasma-facing components (PFCs), e.g., divertor, due to its unique properties to withstand extreme heat. Currently, the ITER council is changing the plasma-facing first-wall material from beryllium to tungsten. The attractiveness of tungsten and its alloys as the most promising plasma-facing candidate (PFC) material, such as for the divertor, lies in its high resistance to plasma-induced sputtering, erosion, and radiation-induced void swelling, together with its high thermal conductivity and high-temperature strength. In ITER, the divertor design includes tungsten mono-blocks for each inner and outer vertical target of a water-cooled cassette assembly [1,2]. In DEMO divertor, the surface heat flux density due to core radiation is expected to be ~1 MW/m^2 [3–5]. However, peak heat flux density in normal operation is expected to reach 10 MW/m^2 and it is expected to be ~20 MW/m^2 during slow transients in the European DEMO divertor [5] The expected lowest shielding temperatures for armour materials vary from ~500 °C in the first wall to >800–900 °C in the proposed helium-cooled divertor designs and >1700 °C on the surface of the deflector armour, while neutron bombardment is evaluated to cause ~8 dpa in the tungsten armour at the end-of-life of PFCs [6,7].

The full-W divertor will operate through the H, He, D and DT phases. Hence, it is important to understand the impact of the various operation phases on the W thermo-mechanical properties [8]. The tungsten armoured divertor will extract most of the helium and other impurities from the DT reaction [2]. The behavior of helium atoms in reactor structural metals has been widely studied due to its catastrophic effect on their radiation resistance and deterioration of their mechanical properties [9]. W-based PFCs exposed to plasma suffer from a variety of radiation-induced lattice damage, surface sputtering, hydrogen isotope retention, helium accumulation, and diffusion into the bulk structure. Helium ion (He^+) irradiation is known to cause the degradation of mechanical and thermal properties via the solution of the atoms within thin layers of tungsten and the subsequent development of nano-scale bubbles which have a significant effect on radiation hardening and

* Corresponding author. Culham Centre for Fusion Energy (CCFE), United Kingdom Atomic Energy Authority (UKAEA), Culham Science Centre, Abingdon, OX14 3DB, United Kingdom.

E-mail addresses: ipatova-julia@yandex.ru, uliia.ipatova@ukaea.uk (I. Ipatova).

https://doi.org/10.1016/j.net.2023.12.003
Received 4 July 2023; Received in revised form 2 November 2023; Accepted 1 December 2023
Available online 5 December 2023

Please cite this article as: I. Ipatova et al., *Nuclear Engineering and Technology*, https://doi.org/10.1016/j.net.2023.12.003

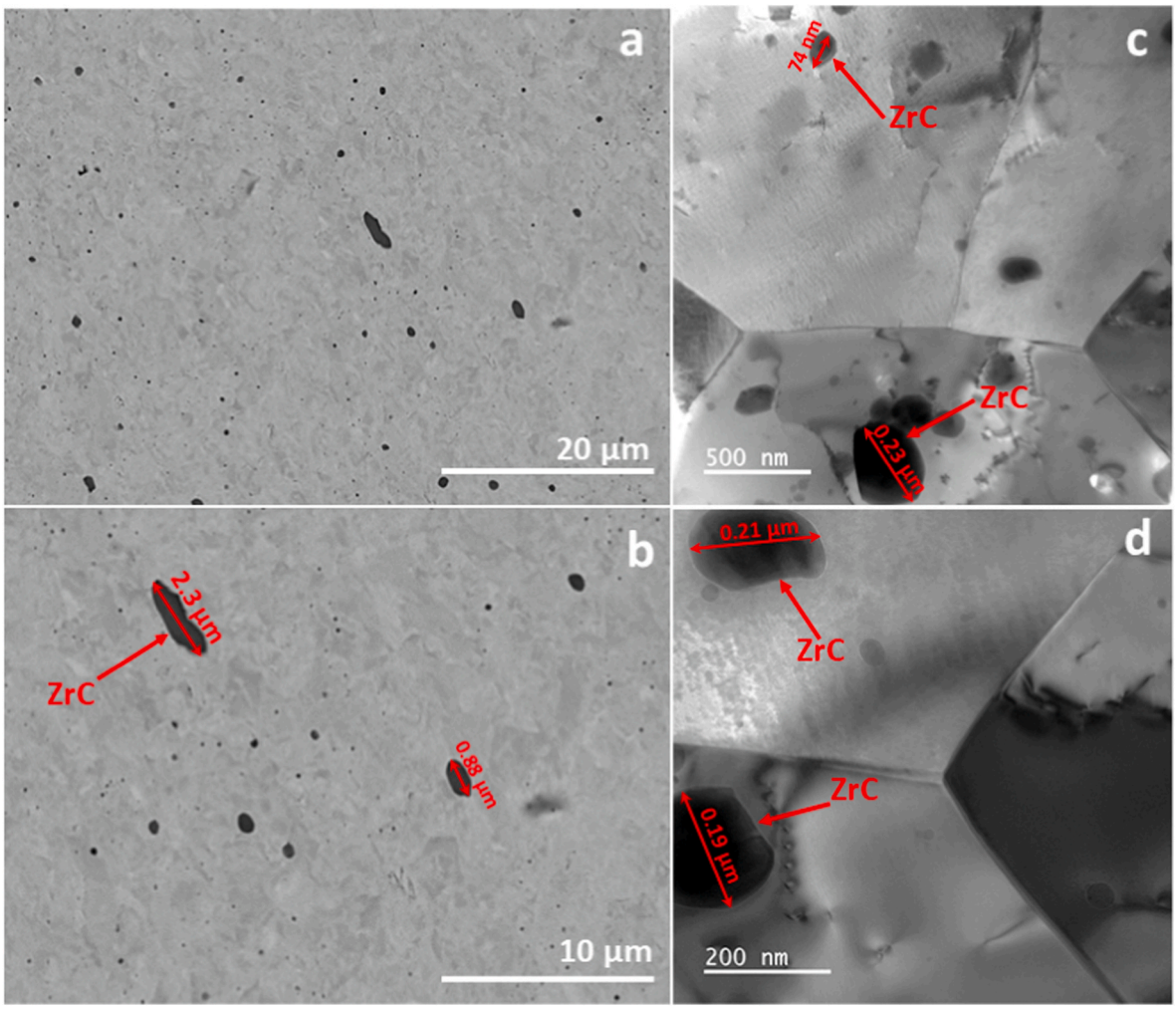

Fig. 1. BSE-SEM images (a, b) and bright-field TEM images (c, d) of W0.5ZrC alloy indicating the size of the secondary phase.

swelling [10]. In addition, exposure of tungsten to He^+ at energies above 20–30 eV, at a minimal fluence of $\sim 10^{25} m^{-2}$ and temperatures >700 °C is known to cause the formation of significant surface changes including surface pores, bubbles, nano-scale tendril-like structures on the surface [11].

Tungsten is known for its extreme brittleness and its high ductile-to-brittle transition temperature (DBTT) which lies in the range of 200–400 °C. This condition may hamper the manufacture of tungsten reactor components and eventually may lead to irreversible catastrophic fracture failure in the course of reactor operations. The successful application of tungsten in fusion reactors will be driven by the reduced DBTT and enhanced fracture toughness as well as higher recrystallisation temperature. One of the potential routes to enhance tungsten properties is alloying tungsten with controlled amounts of other metals or secondary phases to create newly proposed compositions with advanced characteristics. Previous studies on helium irradiation of W and W5wt.%Ta demonstrated that the presence of tantalum impedes the incipient bubble nucleation at high temperatures, preventing premature material swelling, expected in tungsten under helium ions incoming from the plasma [12].

Recently successfully manufactured carbide dispersion strengthened and malleableized tungsten (W) alloys (W0.5ZrC, W1TiC) irradiated with neutrons showed high yield strength and ultimate tensile strength, which can be considered as promising for performance in the high-temperature regime [13–17]. The W0.5ZrC has the lowest DBTT (around 100 °C), and high strength at 600 °C. W1TiC shows a large uniform elongation and capacity for work hardening up to 600 °C. In addition, the TiC nanoparticles were reported to suppress the formation of He bubbles and decreased the void swelling during irradiation of 5-keV He ions at 500 °C, 700 °C, and 900 °C, respectively. The dispersed carbide nanoparticles create a large number of phase interfaces which may act as sinks for irradiation-induced point defects, by enhancing irradiation resistance. Hence, it is possible to expand the temperature window of W by alloying for safe reactor operation and extend the reactor lifetime [18]. Therefore, it is of current interest to test carbide-containing tungsten under various irradiation conditions.

In this study, we performed an in-situ transmission electron microscopy (TEM) study of W and W0.5ZrC exposed to 40 keV He^+ at 800 °C and 1000 °C, to understand the effect of He bubble evolution and the role of ZrC in the this. To unravel and assess the bubble evolution in the presence of ZrC in W as well as to investigate the effects of 0.5 wt%ZrC content on the thermal stability of the microstructure in W, the irradiation has been performed at incremental damage levels from 0.001 dpa up to 1 dpa.

2. Materials

Prior to irradiation experiments, the pristine 1 mm-thick W sheet (99.95 %) was provided by Goodfellow Cambridge Ltd and was annealed in a vacuum furnace at 1400 °C for 2 h. The W0.5ZrC alloy was manufactured and supplied by the Chinese Academy of Sciences in the shape of a plate which was produced by a powder metallurgical process.

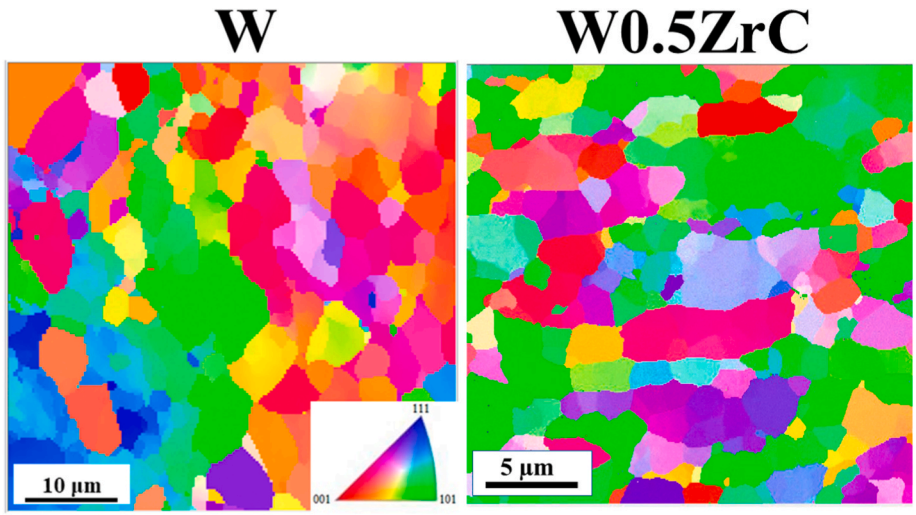

Fig. 2. EBSD map of the **W** and **W0.5ZrC** microstructures prior to helium irradiation.

Table 1
The main parameters used during the 40 keV *in-situ* helium irradiation of W and W0.5ZrC samples at 800 °C and 1000 °C.

Temperature	800 °C/1000 °C
Total irradiation time	6900 s.
Material(s)	W/W0.5ZrC
He^{2+} energy	40 keV
Current (nA)	0.1
Min.-Max. fluence (ions/cm^2)	$3.3 \times 10^{14} \div 7.59 \times 10^{16}$
Flux (ions/cm^2/s)	1.1×10^{13}
Damage rate (dpa/s)	1.5×10^{-4}
Max. damage level	1 dpa

A mixture of tungsten and 0.5 wt% of ZrC nano-sized powders was milled in a high-energy ball mill under a hydrogen atmosphere. The mixed powders were then vacuum sintered at 2200 °C at a pressure of 70 MPa for 20 h, then the process was followed by hot rolling to produce a plate with a thickness of 8.5 mm. To reduce the grain size, the alloy was thermally and mechanically treated through the four-step thermo-mechanical treatment with the deformation steps of 15 %, 20 %, 25 % and 30 %, at 1650 °C) [16,19]. Fig. 1 shows BSE-SEM images (a, b) and bright-field TEM images (c, d) of W0.5ZrC alloy indicating the size of the secondary phase with the red arrows. The ZrC secondary phase has an average size of ~0.6 µm ranging from ~100 nm to 2.3 µm.

The average grain size in W was 3.9 ± 0.8 µm (W) and in W0.5ZrC – 2.1 ± 0.9 µm, see Fig. 2. Both samples were ground down to a thickness of ~100 µm by pre-thinning down from 320 grit to 4000 grit SiC abrasive papers. The obtained thin foils were punched to a disc shape of 3 mm in diameter which were twin-jet electropolished at about −10 °C using a Struers Tenupol-5 unit and an electrolyte comprising an aqueous solution of 2–5 wt% NaOH in water, applying a voltage of 40V.

3. Experimental details

Both W and W0.5ZrC samples have been irradiated with an intense helium beam of 40 keV at MIAMI II Facility, at the University of Huddersfield, where a 300 kV Hitachi H-9500 TEM is coupled to a 350 kV NEC ion accelerator incorporating a Danfysik 921A ion source. The numbers of the implanted and transmitted ions were estimated utilising the Stopping and Range of Ions in Matter (SRIM-13) software [20]. According to the performed calculations, ~56 % of the helium ions were transmitted through the sample foil, and ~32 % were implanted. According to the SRIM predictions, the overall number of ions is 99999, 55531 of those ions were transmitted and 12151 were backscattered.

To reach the target temperature of 800 °C and 1000 °C, a double-tilt heating holder (Gatan Model 652) was used. The samples have been

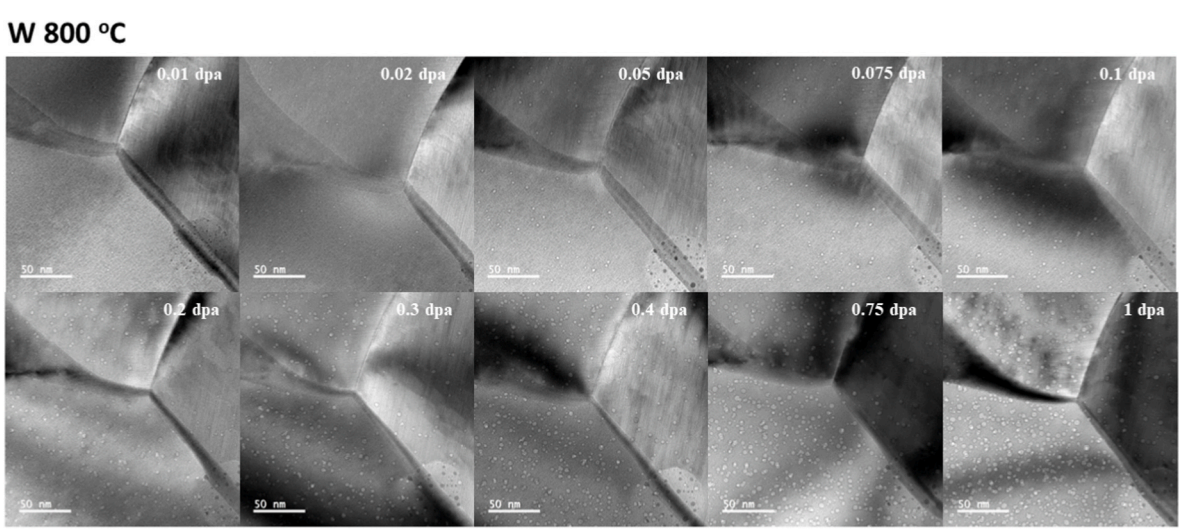

Fig. 3. In-situ observation of the bubble evolution **W** at **800 °C** at selected damage levels up to 1 dpa induced by a 40 keV He^+ ion beam.

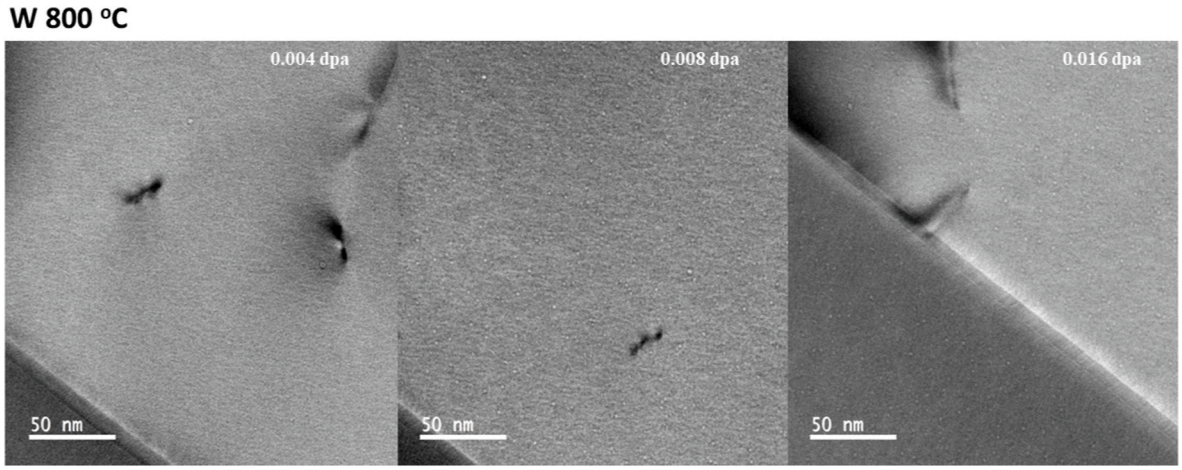

Fig. 4. In-situ observation of bubble formation in **W** at **800 °C** caused by a 40 keV He^{+} ion beam at the relatively low damage levels of: 0.004 dpa, 0.008 dpa, 0.016 dpa.

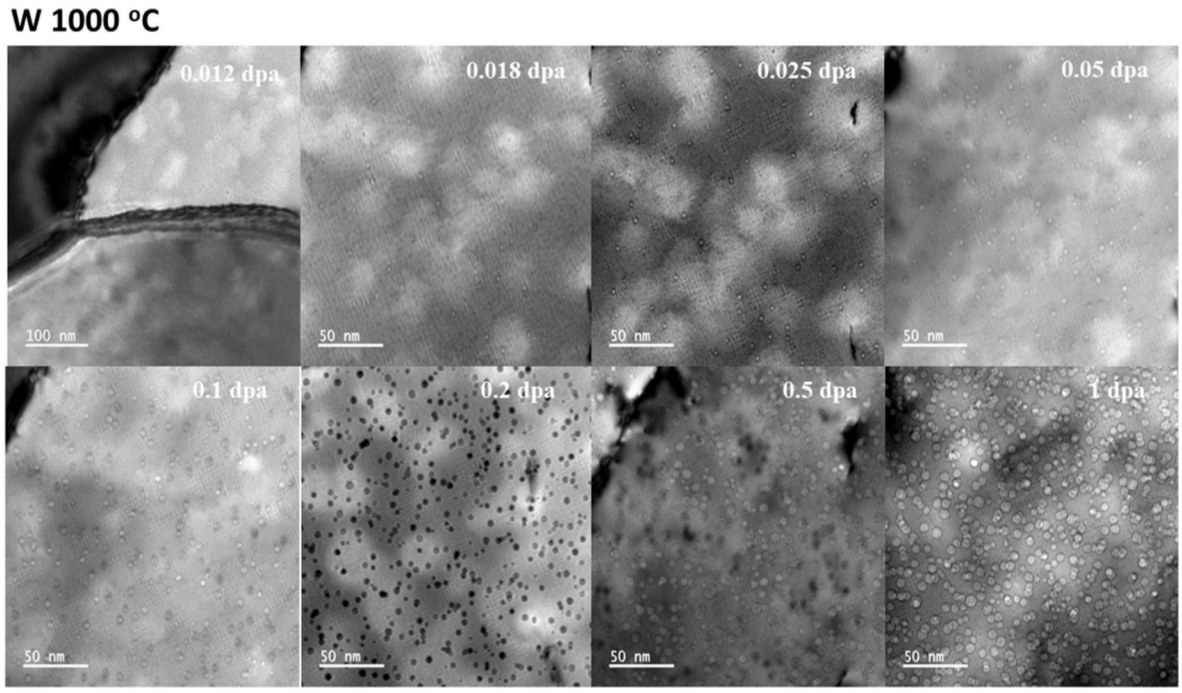

Fig. 5. In-situ observation of the bubble evolution **W** at **1000 °C** at selected damage levels up to 1 dpa induced by a 40 keV He^{+} ion beam.

incrementally irradiated with a helium beam until a damage level of 1 dpa has been reached, corresponding to the helium fluence between 3.3 $\times 10^{14}$ He^{+}/cm^{2} and 7.59 $\times 10^{16}$ He^{+}/cm^{2} (as a maximum at 1 dpa). After each irradiation step the helium beam was switched off in order to analyse the irradiated foil and document images of the defects that occurred at a certain damage level (from 0.09 dpa to 1dpa). Helium bubble production was recorded in under- and over-focus conditions [21]. Micrographs were recorded after each step of the damage level increase. Imaging was performed along the zone axes <111> in W0.5ZrC and <001> in W. At each step of the new defect accumulation, a through-focal series of micrographs was taken with a defocus value $\Delta f \leq 1$ μm to review bubbles of ≥1 nm in diameter. Table 1 contains the main parameters applied during the irradiation experiments. The damage, expressed as displacements per atom (dpa), was calculated with SRIM software with the quick damage options which use Kinchin-Pease formalism, applying an average displacement energy of 90 eV.

The He bubble density was measured from three different zones in each sample and an average value was determined. The local sample thickness was obtained from Convergent Beam Electron Diffraction (CBED) patterns. The thickness of TEM foil was derived by way of the graphical method from the spacing of the fringes of the CBED patterns and was measured to be ~100 nm ± 10 %.

4. Results

In the studied materials, the microstructural damage is defined by nucleated and evolved helium bubbles whose density and morphology change as the damage level increases to a maximum value of 1 dpa. The dislocation loops induced by radiation were absent in both, W and W0.5ZrC, as a consequence of the increased mobility of interstitial atoms at higher temperatures. Previously, dislocation loops of ~3 nm in size have been observed in W0.5ZrC after gold ion irradiation at 600 °C [19]. However, in the course of the in-situ experiments at elevated temperatures, when the diffusion ratio of the point defects is greater, the formed

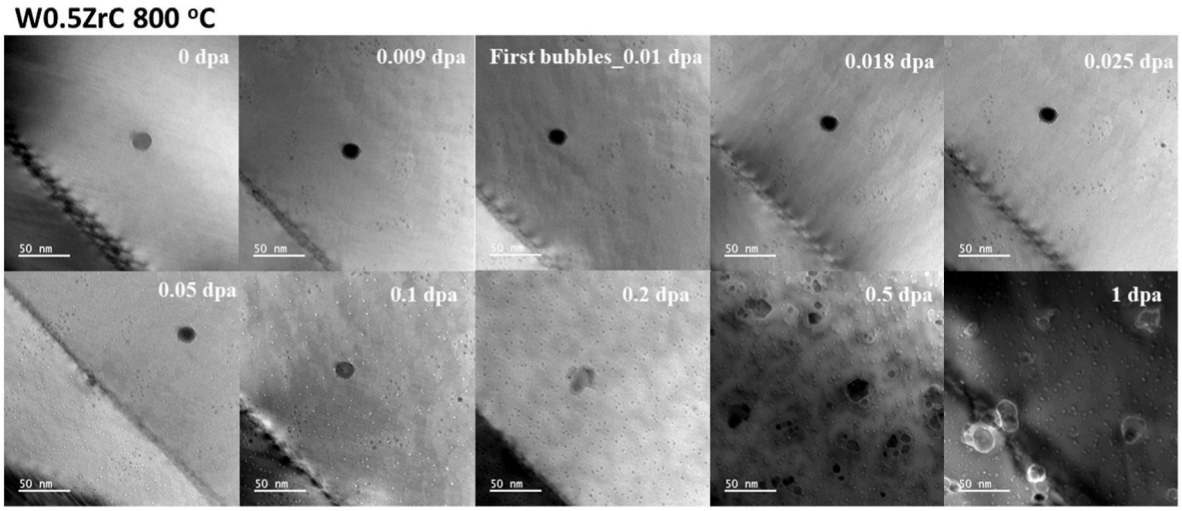

Fig. 6. In-situ observation of the bubble evolution **W0.5ZrC** at **800 °C** at selected damage levels up to 1 dpa induced by a 40 keV He^{+} ion beam.

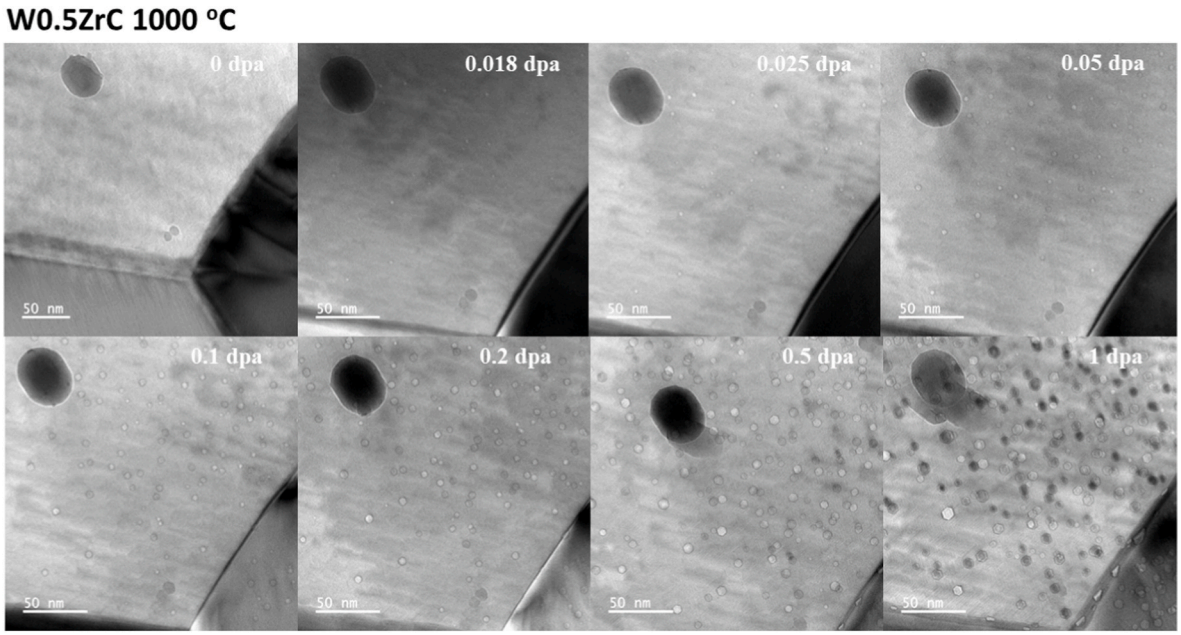

Fig. 7. In-situ observation of the bubble evolution **W0.5ZrC** at **1000 °C** at selected damage levels up to 1 dpa induced by a 40 keV He^{+} ion beam.

loops may self-annihilate at the free sample surfaces [22].

The helium bubble size was measured as the average of 100 bubbles at each condition. The occurrence and evolution of radiation-induced bubbles in W microstructure at 800 °C as a function of damage level in the range between 0.01 and 1 dpa are shown in Fig. 3, whereas the early stages of bubble nucleation formed at 0.004, 0.008, and 0.016 dpa are shown in Fig. 4. At 800 °C, a low number of spherical bubbles of less than 1 nm in diameter was observed in W at the relatively low damage level of 0.004 dpa, which corresponds to a He^{+} fluence of 3.3×10^{14} He^{+}/cm^{2}. The bubbles then gradually grow and reach 3.9 ± 0.4 nm at 1 dpa at 800 °C. At 1000 °C, the first bubbles in W appear at a later stage, namely at 0.012 dpa and their size is > 1 nm. The evolution of the W microstructure at 1000 °C is shown in Fig. 5. The bubbles kept continuously growing and reached 7.1 ± 0.5 nm in size (at 1 dpa), which is 1.8 times bigger than those at 800 °C (Fig. 8). In contrast, the bubble density in W at 1000 °C ($1.5 \pm 0.1 \times 10^{23}$ m^{-3}) is ~2.3 times lower than at 800 °C ($3.2 \pm 0.3 \times 10^{23}$ m^{-3}), see Fig. 8.

Comparatively, Figs. 6 and 7 display the radiation-induced damage in W0.5ZrC in the same damage range as in W, at 800 and 1000 °C respectively. In W0.5ZrC alloy, bubbles were detected at a damage level of 0.01 dpa onwards at both temperatures. At 800 °C, the bubbles in W0.5ZrC saturated in size and stopped growing after 0.5 dpa reaching the size of ~4 nm (see Fig. 8). A higher density of sinks for the irradiation defects in W0.5ZrC promotes defect re-combination and reduces the accumulation and growth of the bubbles at this temperature. At 1000 °C, bubbles in W0.5ZrC kept continuously growing up to ~7 nm in size and the size did not saturate due to absorbing additional mobile vacancies prevailing in the matrix at 1000 °C, when a high vacancy migration takes place. The maximum bubble density in W0.5ZrC at 1000 °C ($1.2 \pm 0.1 \times 10^{23}$ m^{-3}) is close to the one at 800 °C ($1.1 \pm 0.1 \times 10^{23}$ m^{-3}), see Fig. 9, promoting that the bubble density in W is primarily affected by the temperature and addition of ZrC particle into the matrix having an effect on the vacancy mobility and thus their further agglomeration.

The sizes of the bubbles are less than 8 nm in both materials, see Fig. 8. The average bubble size is comparable for both samples at 1 dpa,

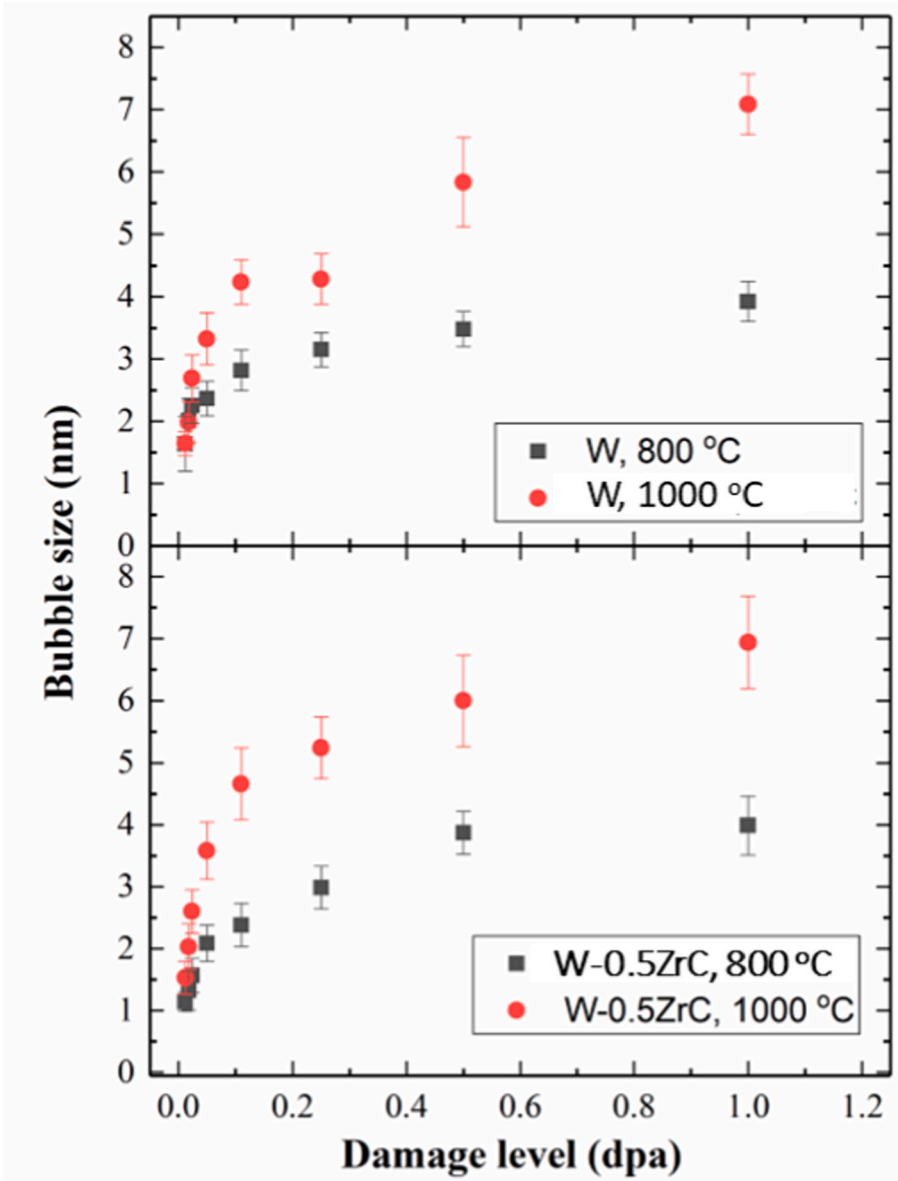

Fig. 8. Average bubble size in **W** and **W0.5ZrC** alloy at **800** °**C** and **1000** °**C** as a function of damage level.

namely, 3.9 ± 0.4 nm (W) and 4 ± 0.5 nm (W0.5ZrC) at 800 °C and 7.1 ± 0.5 nm (W) and 6.9 ± 0.7 nm (W0.5ZrC) at 1000 °C as summarised in Table 2.

In addition, in both materials, the bubbles developed facets and gradually changed their shape from spherical to either quadrilateral and/or hexagonal projections. At 1 dpa, ≥90 % of all the bubbles present in W and W0.5ZrC are faceted at 1000 °C. Some bubbles in W are transitioning from squared to hexagonal prisms (red dotted lines) as they grow, align along the crystallographic planes, and interact with surrounding lattices to minimise the energy associated with their formation. However, at 800 °C, spherical-to-faceted transition in bubble morphology was observed only in W, while in W0.5ZrC most of the helium bubbles remain spherical, and are smaller, as shown in Fig. 10. Interestingly, some of the ZrC particles of 20–50 nm in size have been decorated with the helium bubbles pinned around the particle perimeter. At 1000 °C, a number of faceted bubbles located along high-angle grain boundaries (>20°) can be observed in both samples, see Fig. 11.

At high temperature, higher mobility of radiation-induced defects and grain boundaries with large-angle (>20°) acting as helium sinks/traps may result in facilitating the defect recombination and, hence, annihilation. This explains a lower bubble density in W at a higher temperature and can potentially mitigate helium-induced radiation damage.

5. Discussion

The microstructure of W exposed to helium irradiation is characterised by a large number of bubbles that change in size and density according to the damage level, temperature, and the presence of ZrC particles. There was no evidence of irradiation-induced dislocation loops at 800 °C and 1000 °C due to their instability at the elevated temperatures (~$1/3T_m$). At this temperature range, the dislocation loops tend to emit self-interstitial atoms or glide to the proximate free sample surface in thin sample foils in the in-situ experiments [23].

5.1. Effect of ZrC addition

In general, helium easily migrates in metals by the diffusion of helium atoms with low migration energy (less than 0.1 eV) [24]. Due to its low solubility in metals, helium tends to segregate at microstructural

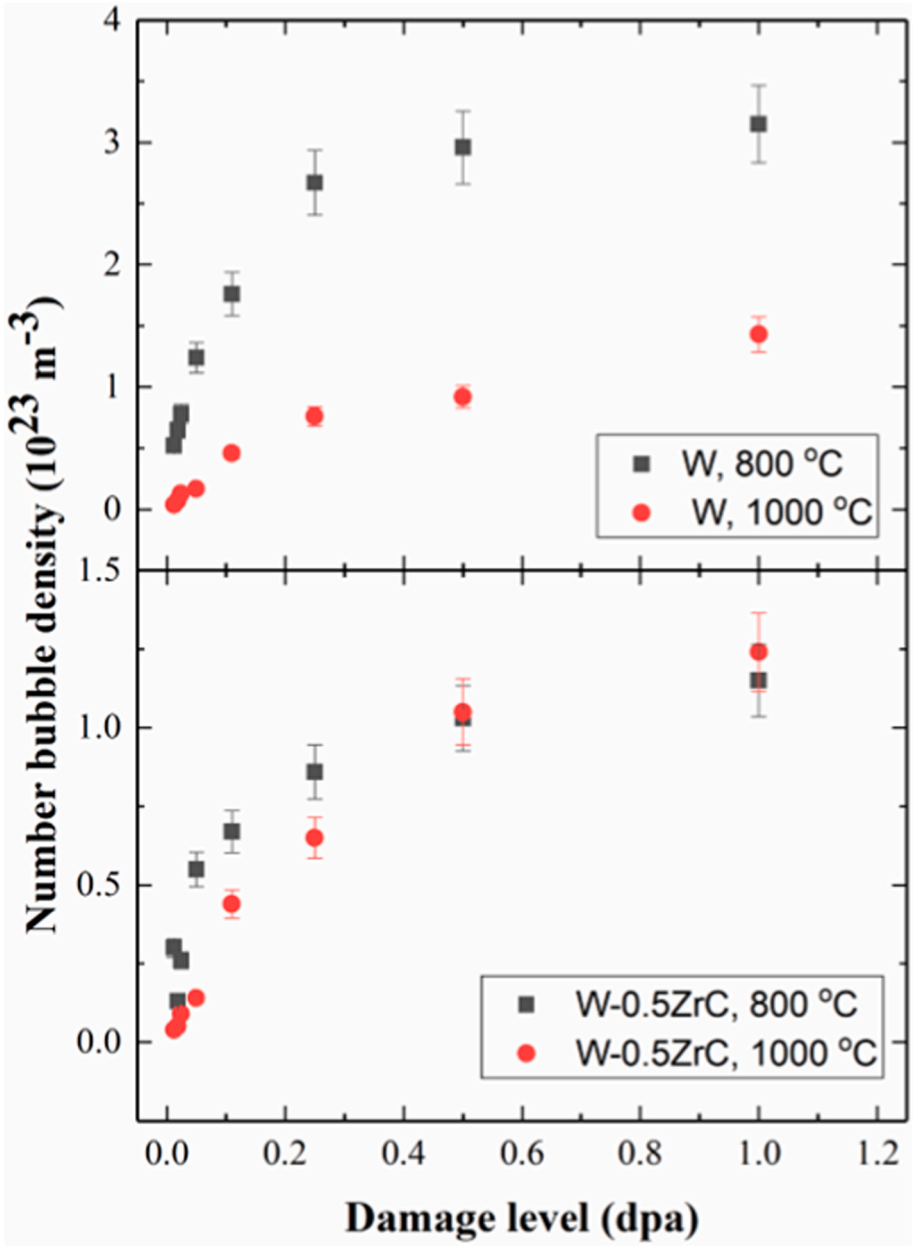

Fig. 9. Average bubble number density in **W** and **W0.5ZrC** alloy at **800 °C** and **1000 °C** as a function of damage level.

Table 2
The main parameters that characterise the population of radiation-induced bubbles observed in W and W0.5ZrC materials at 1 dpa.

Material	Temperature, °C	Average bubble size, nm	Bubble number density, $10^{23}m^{-3}$
W	**800 °C**	3.9 ± 0.4	3.2 ± 0.3
	1000 °C	7.1 ± 0.5	1.5 ± 0.1
W0.5ZrC	**800 °C**	4 ± 0.5	1.1 ± 0.1
	1000 °C	6.9 ± 0.7	1.2 ± 0.1

features. In a crystal lattice, a helium atom usually occupies interstitial and substitutional sites. The preferential site eventually depends on temperature as well as on the presence of other intrinsic or irradiation-induced defects that act as traps for helium atoms [9]. The irradiation temperatures of 800 °C and 1000 °C applied in this study correspond to the annealing stage IV reported for W (i.e., 650–1000 °C) when the radiation-induced vacancies tend to be more mobile [25]. Helium diffusion is essential for bubble formation and growth. Helium atoms are strongly bound with the vacancies because they compensate for their negative volume dilatation [26]. Hence, in pure W, substitutional helium atoms form various strong complexes with vacancies, which are the nuclei of the helium bubbles [27]. The bubble grows with further helium ion and helium-vacancy complex absorption [50]. At higher temperatures ($T > 0.5T_m$), there are two main helium diffusion mechanisms: the general vacancy mechanism leading towards di-vacancy-He transition complexes and the impeded interstitial migration mechanism where a helium atom diffuses interstitially between its thermal dissociation from one vacancy and its re-trapping by another vacancy [28].

The energy barrier of a direct jump of the He atom from one vacancy to another in W was estimated to be quite high (2.8 eV) suggesting a great trapping effect for the W vacancy [29]. At temperatures above 600 °C, the mobility of He vacancy complexes in W increases, which leads to the enlargement of the bubbles to greater than several nanometres in size [30]. Eventually, the implanted He atoms trapped at

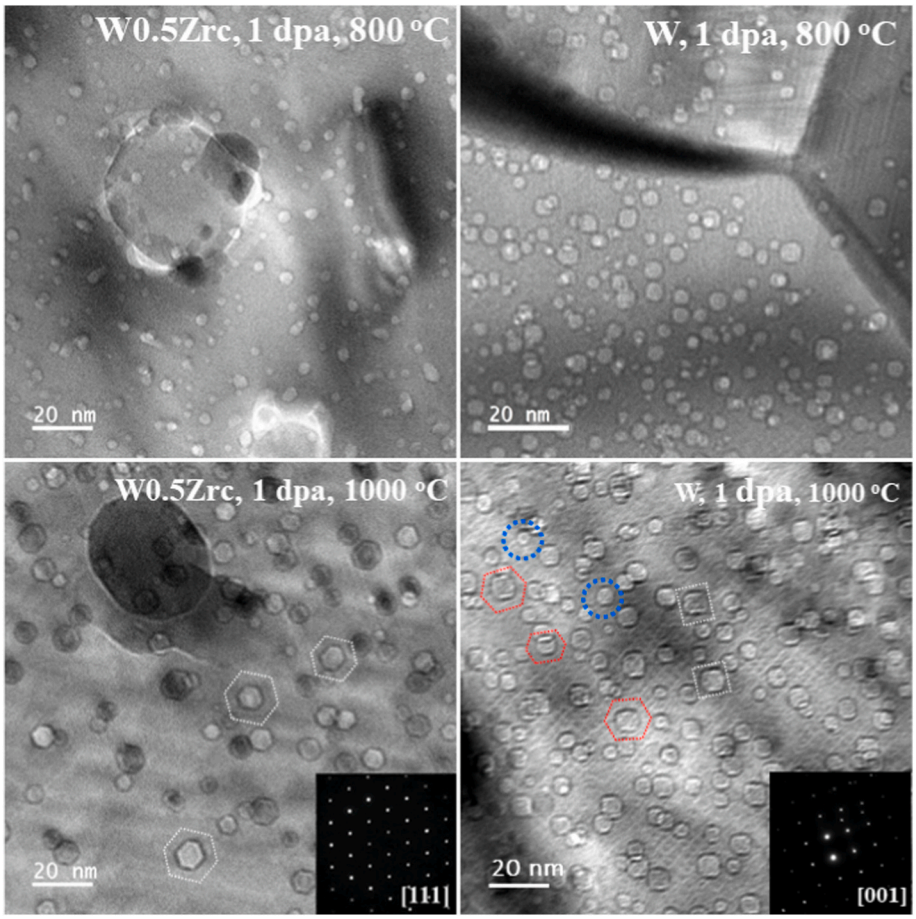

Fig. 10. TEM bright-field images of spherical bubbles in **W0.5ZrC** and faceted bubbles in **W** at **800 °C** at 1 dpa and faceted bubbles in both materials at **1000 °C** at 1 dpa induced by a 40 keV He^{+} ion beam (the dotted lines emphasise the shape of the bubbles).

vacancies become responsible for helium-induced embrittlement. At high doses, helium irradiation causes not only individual atom displacement but also contributes to blistering, pore formation and further cracking, thus serious material degradation.

Single carbon atom prefers to interact with neighbouring W atom at vacancy with the trapping energy of −1.93 eV [31]. Despite the low addition of 0.5 wt% ZrC into W, the present carbon atom tends to reduce the helium-trapping capability of vacancy. This is due to the fact that the binding energy of He to a carbon–vacancy (C–V) complex is weaker than to a C-free vacancy, compromising the helium-trapping capability of the C–V complex in comparison with that of the carbon-free vacancy [32]. These C–V complexes serve as trapping centres for helium reducing the He trapping capability of a vacancy and making the He–V complexes less stable. Therefore, the solute ZrC particles present in the W matrix prevent the formation of vacancy-helium ion complexes, which is a core of a bubble, and, hence, suppress the bubble nucleation. Hence, W0.5ZrC can provide resistance against radiation-induced deformation and damage. This can be especially important in environments where radiation exposure might lead to swelling or creep. In addition, WZrC exhibits relatively low helium retention, which is beneficial for maintaining its mechanical properties in radiation environments [13]. This indicates a higher radiation tolerance of W0.5ZrC to He^{+} implantation.

This trend has been observed in this work during in-situ helium irradiation of W and W0.5ZrC and a similar phenomenon has been previously detected in WTiC alloy [33]. The restriction of the vacancy mobility is found in the bubble density plot in Fig. 9, in which the bubbles occur less frequently in W0.5ZrC than in pure W, suggesting that vacancy-helium clustering and further vacancy capturing are delayed in the alloys due to the carbides present in the matrix. The helium diffusion and solubility in W are low and it has low migration energy. It was shown that second-phase carbon particles play a critical role when dispersed in the W matrix as they enhance the strength of grain boundaries and prevent crack formation and propagation [34]. When a vacancy approaches a carbon atom, it can be energetically favourable for the vacancy to bind to the carbon atom. The carbon atom may attract the vacancy through its electronic structure and its ability to accommodate the missing atom within its vicinity. Vacancies trapped by carbon atoms have reduced mobility and, hence, are less likely to diffuse through the lattice. This may influence various material properties, such as self-diffusion and defect kinetics.

5.2. *Effect of irradiation temperature*

The irradiation temperature has a significant influence on the evolution of radiation-induced microstructure in W, showing a substantial impact on the morphology of the formed bubbles, the number density, and the size, and eventually on the kinetics of their evolution. The main effect of the irradiation temperature increase is primarily related to the type of point defects, their mobility and further interaction, growth, and migration rate within the matrix. It is experimentally proved that the helium bubbles formed in W at elevated temperatures tend to migrate up to the surface and eventually can modify the surface morphology leading to blistering due to the stress around the bubble [35]. The single vacancies in W become mobile at ~300 °C [36]. At higher temperatures, the vacancy clusters, and formed vacancy-helium complexes [37] start migrating and coalescing into larger-size bubbles thus reducing the bubble number density as demonstrated in Figs. 8 and 9. The increased

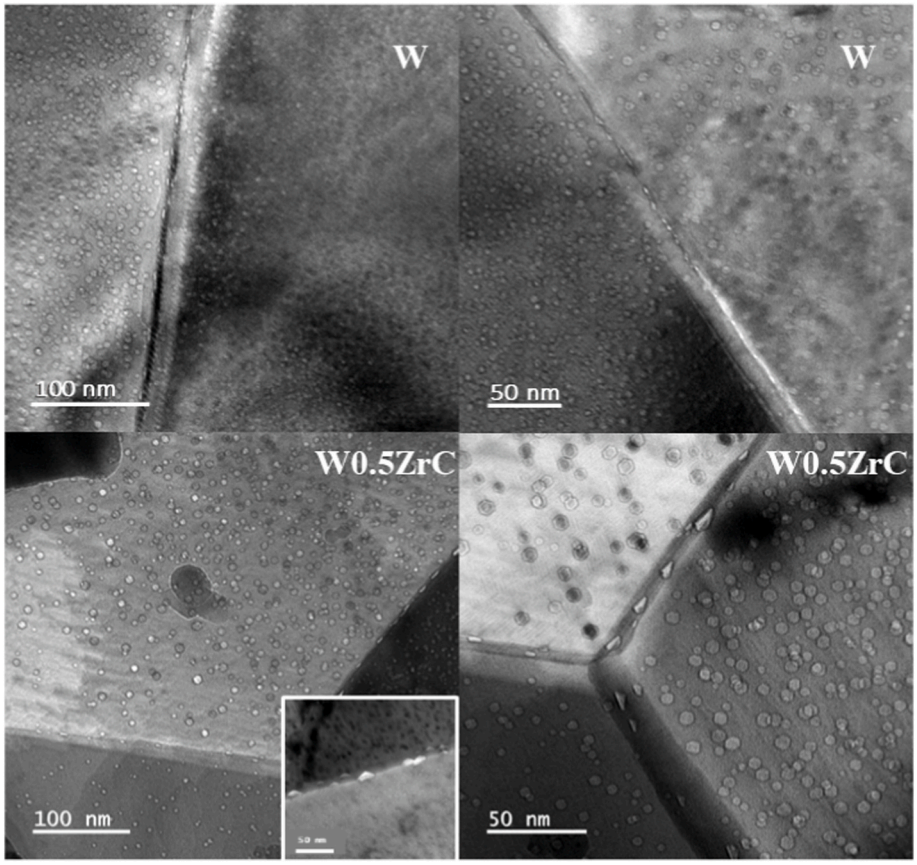

Fig. 11. In-situ TEM bright-field images showing faceted He bubbles along the grain boundaries in **W** and **W0.5ZrC** at **1000 °C**.

kinetic energy of atoms leads to enhanced diffusion of gas atoms to the bubbles' surface. This results in the growth of the nucleated bubbles as the gas atoms accumulate on the bubbles' surface, causing it to expand and grow, hence, promoting the coalescence of nearby bubbles and leading to larger bubbles but of lower bubble density. The bubbles continue growing by absorbing additional mobile vacancies from the matrix, incoming He ions, and helium-vacancy complexes formed during the radiation cascade [37]. Additionally, at 1000 °C, the mobility of vacancy-type defects is enhanced, and the thermal equilibrium concentration of vacancies is reduced as the system dissociates quickly, causing single vacancies to annihilate rather than persist in the system to allow the formation of a bubble. In comparison, in W0.5ZrC, the C atoms hamper the annihilation of vacancy and SIA with the increase in temperature, hence, the density of the bubbles at 1000 °C is slightly higher than at 800 °C. Moreover, the temperature has a significant effect on the possibility of vacancy trapping by carbon atoms due to a higher migration ability of the vacancies at higher temperatures which leads to the prompt vacancy cluster formation [38]. Hence, at elevated irradiation temperatures, the W system containing C atoms creates more vacancies favouring the bubble growth [31].

5.3. The role of grain boundary as helium bubble sinks/traps

Previously it was investigated that He prefers to segregate in the W grain boundary (GB) and it is quite hard for He to dissolve at the W GB due to the positive formation energy of a He atom at the substitutional and interstitial sites in the W GB (3.06 ÷ 6.04 eV). In its turn, the segregation energy is calculated to be – 1.37 eV, indicating that the helium atom will rather segregate in the W GB [39,40]. Therefore, a higher concentration of helium is gathered at the GB regions in W. As more helium atoms accumulate at grain boundaries, they can segregate preferentially along these interfaces. This may lead to helium-related damage growth (bubbles, surface features) near the grain boundaries [41]. This is demonstrated for both materials at 1000 °C in Fig. 11, where helium segregates to the GBs of a higher angle (>20°) in both samples in different areas, forming mostly faceted bubbles along the GBs. Bubble faceting has been demonstrated when a bubble becomes sufficiently large so it can minimise its surface energy by diverging from a spherical shape and by the preferential adsorption of diffusing helium ions on specific plane orientations with respect to the bubble surface [42,43]. The facetted bubbles serve as evidence of the vacancy trapping by the grain boundaries and there is a similar efficiency for simultaneous helium trapping [44]. This segregation of He leads to the W GB expansion affecting the mechanical properties of the W GB. The accumulation of helium can cause embrittlement of the grain boundaries, reducing the material's ductility and fracture toughness. It can also lead to the formation of helium bubbles or bubbles at the grain boundaries, further affecting the material's mechanical behavior. The previous studies of the helium presence at GBs have shown that the cohesion of the system at the GB and the yield stress are consequently decreased with He atoms which are hindering grain boundary sliding upon simple shear [45].

6. Conclusions

In-situ analysis of helium bubble nucleation has been performed in W and W0.5ZrC alloy, induced by 40 keV He^+ irradiation at 800 °C and 1000 °C up to a damage level of 1 dpa. The extensive application of an advanced in-situ TEM characterisation tool showed the effect of helium fluence, temperature, and alloying with ZrC on the dynamics and structural morphology of the forming helium bubbles in the W matrix.

The spherical bubbles of >1 nm in diameter were detected in W at a low damage level of 0.004 dpa, which corresponds to a He^+ fluence of 3.3×10^{14} He^+/cm^2. Additionally, the temperature affected the bubble growth dynamics. The bubbles are more than two times less frequent in

W at 1000 °C than at 800 °C. The particles of ZrC distributed within the W matrix showed suppression of the helium bubble formation, and the first bubbles in W0.5ZrC have been observed at a damage level of 0.01 dpa. Moreover, at 1000 °C, the bubbles in W0.5ZrC are ~7 nm in size and continue growing at expense of absorbing mobile vacancies from the matrix, while at 800 °C, the bubbles' size saturation at ~4 nm was observed in W0.5ZrC.

At 800 °C, and at 1 dpa, the majority of the bubbles in W developed facets, whereas in W0.5ZrC bubbles still represent a spherical shape. At 1000 °C and at 1 dpa, all the present bubbles are faceted in both materials. The bubbles initially formed as spherical embryos showed the progressive transition to a faceted shape at 0.22 dpa. A number of the faceted bubbles observed at 1000 °C were aligned along grain boundaries of a higher angle (>20°) in both samples in various areas of interest.

Declaration of competing interest

The authors declare that they have no known competing financial interests or personal relationships that could have appeared to influence the work reported in this paper.

Acknowledgements

The authors of this work acknowledge Prof S. E. Donnelly for access to the MIAMI-2 facility (grant ref. EPSRC EP/M028283/1) through the EPSRC-funded mid-range facility, the UK National Ion Beam Centre (NS/A000059/1). This work has been part-funded by the EPSRC Energy Programme [grant number EP/W006839/1]. The authors acknowledge Prof Yu Lung Chiu and the Centre for Electron Microscopy at the University of Birmingham for the provided support and assistance.

References

[1] R.A. Pitts, S. Carpentier, F. Escourbiac, T. Hirai, V. Komarov, S. Lisgo, et al., A full tungsten divertor for ITER: physics issues and design status, J. Nucl. Mater. 438 (2013), https://doi.org/10.1016/j.jnucmat.2013.01.008.

[2] T. Hirai, S. Panayotis, V. Barabash, C. Amzallag, F. Escourbiac, A. Durocher, et al., Use of tungsten material for the ITER divertor, Nuclear Materials and Energy 9 (2016) 616–622, https://doi.org/10.1016/j.nme.2016.07.003.

[3] T.R. Barrett, G. Ellwood, G. Pérez, M. Kovari, M. Fursdon, F. Domptail, et al., Progress in the engineering design and assessment of the European DEMO first wall and divertor plasma facing components, Fusion Eng. Des. 109–111 (2016) 917–924, https://doi.org/10.1016/j.fusengdes.2016.01.052.

[4] P. Sardain, B. Michel, L. Giancarli, A. Li Puma, Y. Poitevin, J. Szczepanski, et al., Power plant conceptual study - WCLL concept, Fusion Eng. Des. 69 (2003) 769–774, https://doi.org/10.1016/S0920-3796(03)00146-7.

[5] J.H. You, G. Mazzone, E. Visca, H. Greuner, M. Fursdon, Y. Addab, et al., Divertor of the European DEMO: engineering and technologies for power exhaust, Fusion Eng. Des. 175 (2022), https://doi.org/10.1016/j.fusengdes.2022.113010.

[6] M. Rieth, Advanced Steels, Structural Materials, and High Heat Flux Components, FPCC Meeting, IEA, Paris, 2014.

[7] M. Barbarino, A. Leonard, N.N. Asakura, M. Jakubowski, M. Kobayashi, B. Lipschutz, et al., Summary of the 3rd IAEA Technical Meeting on Divertor Concepts. Nuclear Fusion, vol. 60, Institute of Physics Publishing, 2020, https://doi.org/10.1088/1741-4326/ab9a0c.

[8] G. De Temmerman, T.W. Morgan, G.G. Van Eden, T. De Kruif, M. Wirtz, J. Matejicek, et al., Effect of high-flux H/He plasma exposure on tungsten damage due to transient heat loads, J. Nucl. Mater. 463 (2015) 198–201, https://doi.org/10.1016/j.jnucmat.2014.09.075.

[9] H. Trinkaus, B.N. Singh, C.H. Woo, Defect accumulation under cascade damage conditions, J. Nucl. Mater. 212–215 (1994) 18–28, https://doi.org/10.1016/0022-3115(94)90029-9.

[10] L.M. Dong, N. Gao, Effect of nanoscale helium bubble on nanoindentation in tungsten, Nucl. Instrum. Methods Phys. Res. B 451 (2019) 61–64, https://doi.org/10.1016/J.NIMB.2019.05.012.

[11] M.J. Baldwin, R.P. Doerner, Formation of helium induced nanostructure "fuzz" on various tungsten grades, J. Nucl. Mater. (2010), https://doi.org/10.1016/j.jnucmat.2010.06.034.

[12] I. Ipatova, G. Greaves, S. Pacheco-Gutiérrez, S.C. Middleburgh, M.J.D. Rushton, E. Jimenez-Melero, In-situ TEM investigation of nano-scale helium bubble evolution in tantalum-doped tungsten at 800°C, J. Nucl. Mater. (2021) 550, https://doi.org/10.1016/j.jnucmat.2021.152910.

[13] R. Liu, Z.M. Xie, J.F. Yang, T. Zhang, T. Hao, X.P. Wang, et al., Recent progress on the R&D of W-ZrC alloys for plasma facing components in fusion devices, Nucl. Mater. Energy 16 (2018) 191–206, https://doi.org/10.1016/j.nme.2018.07.002.

[14] T. Zhang, Y.K. Wang, Z.M. Xie, C.S. Liu, Q.F. Fang, Synergistic effects of trace ZrC/Zr on the mechanical properties and microstructure of tungsten as plasma facing materials, Nucl. Mater. Energy 19 (2019) 225–229, https://doi.org/10.1016/j.nme.2019.03.004.

[15] S. Lang, N. Sun, J. Cao, W. Yu, Z. Yang, S. Hou, Fabrication of ultra-fine-grained w-tic alloys by a simple ball-milling and hydrogen reduction method, Materials 14 (2021) 1–12, https://doi.org/10.3390/ma14195865.

[16] Z.M. Xie, R. Liu, S. Miao, X.D. Yang, T. Zhang, X.P. Wang, et al., Extraordinary high ductility/strength of the interface designed bulk W-ZrC alloy plate at relatively low temperature, Sci. Rep. 5 (2015) 1–11, https://doi.org/10.1038/srep16014.

[17] Zhang T, Xie Z, Liu C, Xiong Y. The Tungsten-Based Plasma- Facing Materials N.d.: 1–19. .

[18] J. Linke, J. Du, T. Loewenhoff, G. Pintsuk, B. Spilker, I. Steudel, et al., Challenges for plasma-facing components in nuclear fusion, Matter Radiat. Extremes 4 (2019), https://doi.org/10.1063/1.5090100.

[19] W. Van Renterghem, D. Terentyev, S. Balaji, C. David, A. Dubinko, C. Yin, et al., Microstructural evolution in pure and ZrC strengthened tungsten under ion irradiation at 600°C, J. Nucl. Mater. 544 (2021), 152710, https://doi.org/10.1016/j.jnucmat.2020.152710.

[20] R.~E. Stoller, M.~B. Toloczko, G.~S. Was, A.~G. Certain, S. Dwaraknath, F.~A. Garner, On the use of SRIM for computing radiation damage exposure, Nucl. Instrum. Methods Phys. Res. B 310 (2013) 75–80, https://doi.org/10.1016/j.nimb.2013.05.008.

[21] M.L. Jenkins, Characterisation of radiation-damage microstructures by TEM, J. Nucl. Mater. 216 (1994) 124–156, https://doi.org/10.1016/0022-3115(94)90010-8.

[22] R.W. Harrison, N. Peng, R.P. Webb, J.A. Hinks, S.E. Donnelly, Characterisation of helium ion irradiated bulk tungsten: a comparison with the in-situ TEM technique, Fusion Eng. Des. 138 (2019) 210–216, https://doi.org/10.1016/j.fusengdes.2018.11.024.

[23] I. Ipatova, R.W. Harrison, D. Terentyev, S.E. Donnelly, E. Jimenez-Melero, Thermal evolution of the proton irradiated structure in tungsten–5 wt% tantalum, J. Fusion Energy 36 (2017), https://doi.org/10.1007/s10894-017-0145-y.

[24] J.E. Nathaniel, O. El-Atwani, S. Huang, J. Marian, A.C. Leff, J.K. Baldwin, et al., Implications of microstructure in helium-implanted nanocrystalline metals, Materials 15 (2022), https://doi.org/10.3390/ma15124092.

[25] L.K. Keys, J. Moteff, Neutron irradiation and defect recovery of tungsten, J. Nucl. Mater. 34 (1970) 260–280, https://doi.org/10.1016/0022-3115(70)90193-5.

[26] G.D. Samolyuk, Y.N. Osetsky, R.E. Stoller, Properties of vacancy complexes with hydrogen and helium atoms in tungsten from first principles, Fusion Sci. Technol. 71 (2017) 52–59, https://doi.org/10.13182/FST16-118.

[27] D. Perez, L. Sandoval, S. Blondel, B.D. Wirth, B.P. Uberuaga, A.F. Voter, The mobility of small vacancy/helium complexes in tungsten and its impact on retention in fusion-relevant conditions, Sci. Rep. 7 (2017), https://doi.org/10.1038/s41598-017-02428-2.

[28] H. Trinkaus, B.N. Singh, Helium accumulation in metals during irradiation – where do we stand? J. Nucl. Mater. 323 (2003) 229–242, https://doi.org/10.1016/J.JNUCMAT.2003.09.001.

[29] C. González, R. Iglesias, Migration mechanisms of helium in copper and tungsten, J. Mater. Sci. 49 (2014) 8127–8139, https://doi.org/10.1007/s10853-014-8522-7.

[30] Y. Ueda, J.W. Coenen, G. De Temmerman, R.P. Doerner, J. Linke, V. Philipps, et al., Research status and issues of tungsten plasma facing materials for ITER and beyond, Fusion Eng. Des. 89 (2014) 901–906, https://doi.org/10.1016/J.FUSENGDES.2014.02.078.

[31] Y.L. Liu, H.B. Zhou, Y. Zhang, G.H. Lu, G.N. Luo, Interaction of C with vacancy in W: a first-principles study, Comput. Mater. Sci. 50 (2011) 3213–3217, https://doi.org/10.1016/j.commatsci.2011.06.003.

[32] H.B. Zhou, X. Ou, Y. Zhang, X. Shu, Y.L. Liu, G.H. Lu, Effect of carbon on helium trapping in tungsten: a first-principles investigation, J. Nucl. Mater. 440 (2013) 338–343, https://doi.org/10.1016/j.jnucmat.2013.05.070.

[33] Q. Xu, X.Y. Ding, L.M. Luo, M. Miyamoto, M. Tokitani, J. Zhang, et al., Thermal stability and evolution of microstructures induced by He irradiation in W–TiC alloys, Nucl. Mater. Energy 15 (2018) 76–79, https://doi.org/10.1016/j.nme.2018.02.003.

[34] X.-Y. Tan, P. Li, L.-M. Luo, Q. Xu, K. Tokunaga, X. Zan, et al., Effect of second-phase particles on the properties of W-based materials under high-heat loading, Nucl. Mater. Energy 9 (2016) 399–404, https://doi.org/10.1016/j.nme.2016.07.009.

[35] H. Zhang, J. Sun, Y. Wang, M. Qin, T. Stirner, Molecular dynamics simulation analysis of the stress around an up-migrating helium bubble under tungsten surface and its bursting, SSRN Electron. J. (2022), https://doi.org/10.2139/ssrn.4037115.

[36] A. Debelle, M.F. Barthe, T. Sauvage, First temperature stage evolution of irradiation-induced defects in tungsten studied by positron annihilation spectroscopy, J. Nucl. Mater. 376 (2008) 216–221, https://doi.org/10.1016/j.jnucmat.2008.03.002.

[37] X.C. Li, Y.N. Liu, Y. Yu, G.N. Luo, X. Shu, G.H. Lu, Helium defects interactions and mechanism of helium bubble growth in tungsten: a molecular dynamics simulation, J. Nucl. Mater. 451 (2014) 356–360, https://doi.org/10.1016/j.jnucmat.2014.04.022.

[38] Y.-Z. Niu, Y.-H. Li, Q.-Y. Ren, Z.-Z. Li, D. Terentyev, H.-Z. Ma, et al., Influence of carbon on the evolution of irradiation defects in tungsten, J. Nucl. Mater. (2023), 154393, https://doi.org/10.1016/j.jnucmat.2023.154393.

[39] H.B. Zhou, Y.L. Liu, Y. Zhang, S. Jin, G.H. Lu, First-principles investigation of energetics and site preference of He in a W grain boundary, Nucl. Instrum. Methods Phys. Res. B 267 (2009) 3189–3192, https://doi.org/10.1016/j.nimb.2009.06.067.

[40] L. Hu, K.D. Hammond, B.D. Wirth, D. Maroudas, Interactions of mobile helium clusters with surfaces and grain boundaries of plasma-exposed tungsten, J. Appl. Phys. 115 (2014), https://doi.org/10.1063/1.4874675.

[41] K.D. Hammond, L. Hu, D. Maroudas, B.D. Wirth, Helium impurity transport on grain boundaries: enhanced or inhibited? EPL 110 (2015) https://doi.org/10.1209/0295-5075/110/52002.

[42] K. Niwase, T. Ezawa, F.E. Fujita, H. Kusanagi, H. Takaku, Morphology of micro-cavities in nickel during Helium bombardment and post-irradiation annealing, Radiat. Eff. 106 (1988) 65–76, https://doi.org/10.1080/00337578808013729.

[43] Z.J. Bergstrom, D. Perez, O. El-Atwani, Helium bubble facetation in tungsten thin films, Scripta Mater. 220 (2022), https://doi.org/10.1016/j.scriptamat.2022.114918.

[44] O. El-Atwani, J.A. Hinks, G. Greaves, J.P. Allain, S.A. Maloy, Grain size threshold for enhanced irradiation resistance in nanocrystalline and ultrafine tungsten, Mater. Res. Lett. 5 (2017) 343–349, https://doi.org/10.1080/21663831.2017.1292326.

[45] E. Martinez, B.P. Uberuaga, B.D. Wirth, Atomistic modeling of helium segregation to grain boundaries in tungsten and its effect on de-cohesion, Nucl. Fusion 57 (2017), https://doi.org/10.1088/1741-4326/aa6e15.